

# MicroMix: Efficient Mixed-Precision Quantization with Microscaling Formats for Large Language Models

Wenyuan Liu<sup>1</sup>, Haoqian Meng<sup>1</sup>, Yilun Luo<sup>1</sup>, Peng Zhang<sup>1\*</sup>, Xindian Ma<sup>1</sup>

<sup>1</sup> College of Intelligence and Computing, Tianjin University, Tianjin, China

## Abstract

Quantization significantly accelerates inference in large language models (LLMs) by replacing original high-precision matrices with low-precision counterparts. Recent advances in weight-activation quantization have primarily focused on mapping both weights and activations to the INT4 format. Although the new FP4 Tensor Cores in NVIDIA’s Blackwell architecture offer up to 4x speedup over FP16, existing INT4-based kernels fail to fully exploit this capability due to mismatched data formats. To bridge this gap, we propose MicroMix, a co-designed mixed-precision quantization algorithm and matrix multiplication kernel based on Microscaling (MX) data formats. Tailored for the Blackwell architecture, the MicroMix kernel supports arbitrary combinations of MXFP4, MXFP6, and MXFP8 channels, and produces BFloat16 outputs. To achieve a favorable trade-off between accuracy and efficiency for each linear layer, we introduce quantization thresholds that identify activation elements where lower-precision formats (MXFP4 or MXFP6) incur excessive quantization error. Our algorithm selectively allocates higher-precision channels to preserve accuracy while maintaining compute efficiency. MicroMix achieves competitive or superior performance across diverse downstream tasks, including zero-shot and few-shot learning, language modeling, code generation, and mathematical reasoning. On both consumer-grade (RTX 5070Ti laptop) and server-grade (RTX 5090) GPUs, our kernel delivers at least 20% faster execution than TensorRT-FP8. Furthermore, when applied to various Llama and Qwen models, MicroMix consistently improves prefill latency and memory efficiency across a range of batch sizes compared to TensorRT baselines. Our code is available at <https://github.com/lwy2020/MicroMix.git>.

## 1 Introduction

In recent years, large language models (LLMs) have demonstrated remarkable performance across a wide range of tasks (Vaswani et al. 2023; Brown et al. 2020). However, these capabilities come with substantial computational and energy costs. To mitigate this, quantization techniques replace high-precision matrix multiplications with more efficient low-bit alternatives (Yao et al. 2022; Xiao et al. 2024; Shen et al. 2023), significantly improving LLM inference speed.

Quantization techniques are broadly classified into weight-only and weight-activation approaches. Weight-only

methods (Lin et al. 2024; Frantar et al. 2023) have substantially mitigated the precision loss associated with 4-bit weights and 16-bit activations (W4A16). In parallel, weight-activation methods (Dettmers et al. 2022; Xiao et al. 2024) suppress activation outliers effectively, enabling accurate 8-bit quantization of both weights and activations (W8A8). More recently, mixed-precision and rotation-based quantization algorithms (Ashkboos et al. 2024; Zhao et al. 2024) have pushed the frontier further to W4A4, achieving strong performance on downstream tasks.

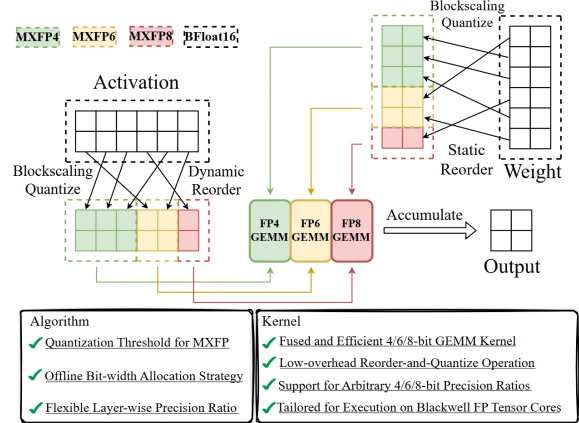


Figure 1: Overview of MicroMix. MicroMix assigns different bit-widths to individual channels, allocating higher precision to channels with larger absolute mean values. For activations, channel reordering is performed online using indices derived from a calibration dataset. In contrast, weights are reordered and quantized offline, with the transformation applied only once.

Despite these advances, two key bottlenecks continue to restrict the kernel-level efficiency of INT4-based quantization: (1) The widely adopted group-wise integer quantization scheme requires dequantizing each integer group to floating-point values followed by partial summations. This procedure is executed on slower CUDA Cores, as INT8 Tensor Cores only support INT32 accumulation. (2) NVIDIA’s latest Blackwell architecture introduces FP4 Tensor Cores that offer up to 4x higher throughput than FP16 and 2x higher than FP8 or INT8. However, existing INT-based

\*Corresponding Author: Peng Zhang <pzhang@tju.edu.cn>

quantization kernels are incompatible with these new tensor cores and thus fail to leverage their full potential. As a result, significant room remains for optimizing quantization kernel throughput on the Blackwell architecture.

Microscaling (MX) data formats such as MXFP8, MXFP6, and MXFP4 offer a efficient open standard for deep learning (Darvish Rouhani et al. 2023a). By integrating floating-point representations with fine-grained block-wise quantization and hardware-supported dequantization, these formats are well suited to exploit the FP Tensor Cores introduced in NVIDIA’s Blackwell architecture. Despite their potential, quantization kernels targeting MX formats, especially those supporting mixed precision, have received limited attention. When existing mixed-precision quantization algorithms are directly applied to MX formats, they often lead to noticeable accuracy degradation. This degradation primarily results from assigning a fixed number of high-precision channels to all activations, without adapting to the diverse quantization error inherent to MX formats and further amplified by the diversity of activation distributions.

In this paper, we propose MicroMix, a mixed-precision quantization framework based on Microscaling (MX) data formats, featuring a co-designed algorithm and kernel. MicroMix is built upon three key components: **(1) Efficient reorder-and-quantize operation.** To address performance degradation caused by irregular memory access patterns, we integrate a reorder step directly into the mixed-precision quantization kernel. This design enables high-throughput quantization across heterogeneous precision levels without introducing additional overhead. **(2) Flexible bit-width ratios (4, 6, and 8 bits).** Our quantization kernel supports multiple data formats (MXFP8, MXFP6, MXFP4) and arbitrary mixing ratios. By integrating with CUTLASS GEMM, we instantiate optimized matrix multiplication kernels tailored to specific data types and problem sizes. In addition, dequantization operations are deeply fused into the MMA instructions, ensuring negligible additional overhead on Blackwell Tensor Cores. **(3) Low-error precision assignment strategy.** We propose a bit assignment algorithm that adapts to the different input distributions from the perspective of quantization error. The core idea is to ensure that the quantization error of lower-bit formats stays below the error upper bound of higher-precision formats. To achieve this, we define quantization thresholds for MXFP4 and MXFP6: elements that exceed the threshold at a given target bit-width are reassigned to higher-precision formats to preserve model accuracy. This formula introduces explicit outlier thresholds for MXFP4 and MXFP6, addressing a limitation in prior work where such definitions were absent.

We evaluate MicroMix on multiple downstream tasks, including zero-shot and few-shot learning, language modeling, code generation and mathematical reasoning. Across various Llama and Qwen models, MicroMix achieves accuracy that is comparable to or better than state-of-the-art baselines. For efficiency analysis, we test MicroMix on both a consumer-grade RTX 5070Ti laptop and a server-grade RTX 5090 GPU. Compared to TensorRT-FP8, MicroMix accelerates kernel-level computation by 8% to 46% on the RTX 5070Ti laptop and by 16% to 46% on the RTX 5090.

When deployed within transformer blocks, MicroMix improves layer-wise execution speed by 6% to 29%, and boosts end-to-end throughput by 3% to 9%, consistently outperforming TensorRT-FP8 across a range of configurations.

## 2 Preliminary and Motivations

### 2.1 Preliminary

The basic unit of Microscaling data formats (MX) is a block of size  $k$ , consisting of  $k$  scalar elements  $\{X_j\}_{j=1}^k$  and a single shared scaling factor  $s$  in E8M0 (Darvish Rouhani et al. 2023a). Given a FP16 tensor  $\mathbf{X} \in \mathbb{R}^{1 \times I}$ , quantization to MXFP8/MXFP6/MXFP4 first partitions  $\mathbf{X}$  into blocks of 32 elements  $\{X_i\}_{i=1}^N$ ,  $N = \frac{I}{32}$ , then applies per-block symmetric quantization for  $\forall X_j \in \mathbf{X}_i$  as follows:

$$Q(X_j) = \text{round}\left(\frac{X_j}{s}\right), s = 2^{\lfloor \log_2(\max(|X_i|)) \rfloor - b} \quad (1)$$

where  $\text{round}(\cdot)$  denotes rounding to the nearest MXFP value and the exponent bias  $b$  is format-specific (see Appendix A for more details).

After quantizing both weight and activation using Equation (1), the original matrix multiplication can be approximated by a low-precision computation:

$$\mathbf{Y} = \mathbf{X}\mathbf{W} \approx Q(\mathbf{X})Q(\mathbf{W}) \cdot s_{\mathbf{X}}s_{\mathbf{W}} \quad (2)$$

where  $s_{\mathbf{X}}$  and  $s_{\mathbf{W}}$  are the scaling factors of  $\mathbf{X}$  and  $\mathbf{W}$  respectively. Given a tensor  $\mathbf{X}$ ,  $\forall X_j \in \mathbf{X}$ , the quantization error for  $X_j$  is defined as:

$$E(X_j) = |X_j - Q(X_j)| = |X_j - \text{round}\left(\frac{X_j}{s}\right)| = \gamma \cdot s \quad (3)$$

where  $\gamma = |\text{round}(X_j/s) - X_j/s|$  is the rounding error.

In Appendix B.1, we further analyze the relationship between quantization error and model accuracy. Empirically, we observe that model accuracy remains close to the FP16 baseline as long as the quantization error is constrained within a specific threshold. However, once the quantization error exceeds this threshold, accuracy degrades rapidly. For recent LLMs, INT8 quantization typically remains within the high-accuracy region, whereas INT4 often lies near the onset of significant accuracy degradation.

### 2.2 Motivations

The primary motivations of this paper stem from addressing the limitations in current quantization methods and their corresponding kernels.

**Motivation 1: Adaptive Mixed-precision Allocation for Diverse Activation Distributions.** Existing mixed-precision quantization methods such as Atom (Zhao et al. 2024), employ a fixed number of high-precision channels across all layers. This uniform allocation fails to account for the heterogeneous activation distributions observed in different layers (see Figure 2). Specifically, layers with larger activation values across channels require more high-precision channels to reduce the quantization error. Consequently, directly applying current fixed-allocation mixed-precision algorithms to MX formats leads to a noticeable degradation

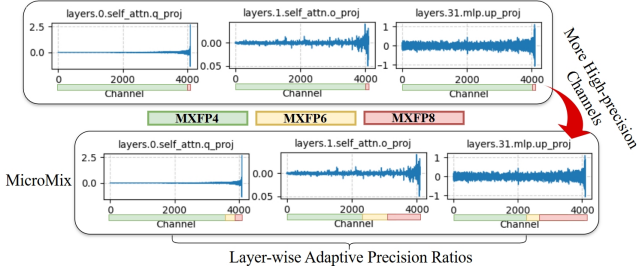


Figure 2: Channel-wise mean values of three activation tensors from Llama3.1-8B, with outlier channels reordered to the end. Compared to prior methods, MicroMix assigns a larger portion of channels to higher-precision formats and applies layer-wise adaptive precision ratios across all linear layers.

in accuracy (see Appendix C.2). To overcome this, we propose a novel strategy that flexibly allocates the number of 4, 6, and 8-bit channels per layer. This adaptive approach ensures that all linear layers consistently maintain low errors, thereby improving model accuracy.

**Motivation 2: Leveraging FP4 Tensor Cores for Enhanced Kernel Efficiency.** Current INT-based kernels, exemplified by Atom and QuaRot (Ashkboos et al. 2024), require dequantization on CUDA Cores because INT8 Tensor Cores only produce INT32 partial sums. As illustrated in Figure 3, the dequantization process on CUDA Cores, particularly the conversion from INT32 to FP32, consumes approximately 85% of the total execution time on RTX 5090, severely limiting the performance of these INT kernels on Blackwell architecture. In stark contrast, FP4 matrix multiplication allows for direct dequantization on FP4 Tensor Cores, leading to a significant improvement in computational efficiency. This fundamental advantage highlights the critical need for developing next-generation mixed-precision methods with kernels specifically designed for FP formats.

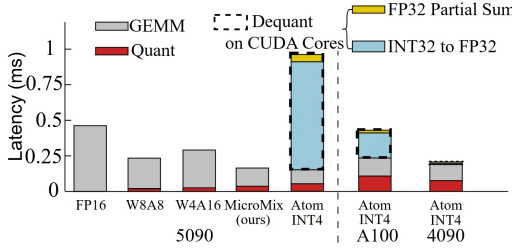


Figure 3: Runtime breakdown of five matrix multiplication kernels on RTX 5090, A100, and RTX 4090 GPUs. The FP16, W8A8 (FP8) and W4A16 kernels are implemented using TensorRT-LLM. For both TensorRT-LLM and MicroMix, the dequantization operations are fused within the GEMM kernel. The input matrix dimensions are 2048×4096 and 4096×4096.

**Motivation 3: Quantization Error Management through Adaptive Thresholding for Outliers.** Quantization error, inherent to the format conversion between

original activations  $\mathbf{X}$  and their quantized representations  $Q(\mathbf{X})$ , cannot be entirely eliminated. Therefore, it is critical to ensure this error remains within an acceptable bound. While prior works have introduced various techniques, such as smoothing, rotation, and clipping, to mitigate the impact of outliers in activations. There is still a notable gap in research concerning the precise threshold above which outliers should be constrained for MXFP4 and MXFP6. In this paper, we define specific quantization thresholds for MXFP4 and MXFP6 formats. Elements exceeding these defined thresholds will be preferentially stored in MXFP8, thereby effectively minimizing quantization error and maintaining high model fidelity.

### 3 Method

To address the accuracy degradation commonly observed in INT4 quantized models on downstream tasks, prior work has explored various solutions. However, post-training quantization for Microscaling (MX) formats remains underexplored. Leveraging the inherent flexibility of multiple MX data formats, we propose MicroMix, a novel co-designed mixed-precision quantization algorithm and kernel.

#### 3.1 Algorithm

In MicroMix, we partition the activation tensor channels into three groups:  $\mathbf{P}_4$ ,  $\mathbf{P}_6$ , and  $\mathbf{P}_8$ , which are then quantized to MXFP4, MXFP6, and MXFP8, respectively. The corresponding weight channels are quantized to the same bit-width as their activation counterparts. Our method is structured around addressing three key questions:

**Q1: How do we determine the optimal proportion for each precision level?** Our core idea is to ensure that the quantization errors introduced by MXFP4 and MXFP6 do not exceed the upper bound of the quantization error associated with standard INT8:

$$E(X_j)_{\{\text{MXFP4, MXFP6}\}} \leq \bar{E}(X_j)_{\text{INT8}} \quad (4)$$

The goal of this constraint is to store elements that cause excessive quantization error at their target bit-width (MXFP4, MXFP6) in higher precision (MXFP6, MXFP8). To precisely distinguish outliers from other elements, we define the quantization threshold as follows:

**Definition 1.** Given a high-precision bit-width (e.g., 8-bit for recent LLMs) and a target bit-width  $n$ , the quantization threshold  $T(n)$  is defined as:

$$T(n) = 2^b \cdot \frac{2^{n-1}}{q_{\max}} \cdot \bar{E}(X_j)_{\text{INT8}} = 2^{b+n-1} \cdot \frac{\max(|\mathbf{X}|)}{254 \cdot q_{\max}} \quad (5)$$

To maintain low quantization error at MXFP4 or MXFP6, the maximum allowable magnitude within group must satisfy:

$$\max(|\mathbf{P}_n|) \leq T(n) \quad (6)$$

Here,  $n$  denotes the number of bits,  $b$  is the exponent bias and  $q_{\max}$  represents the maximum representable value in the target format. A detailed derivation of the quantization threshold is provided in Appendix B.2.

**Q2: What are the characteristics of the proportions of each part?** We calculate the proportions  $p_4$ ,  $p_6$ , and  $p_8$  corresponding to the channel groups  $\mathbf{P}_4$ ,  $\mathbf{P}_6$ , and  $\mathbf{P}_8$  for each

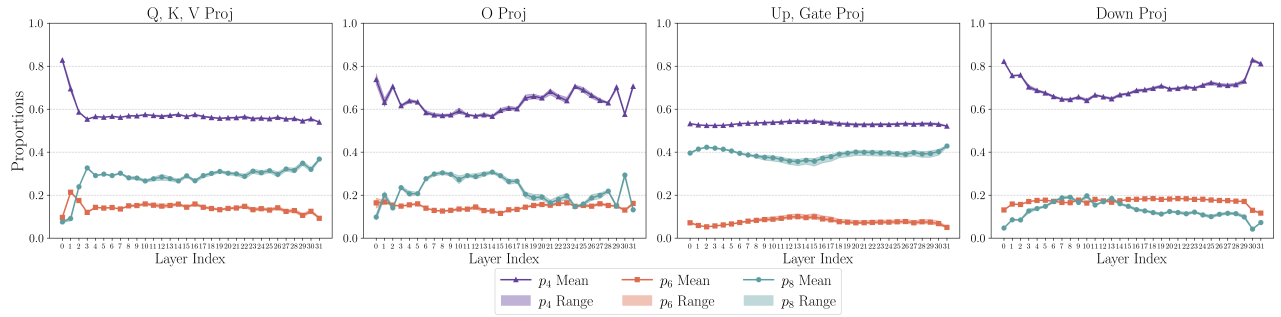


Figure 4: Distribution statistics of  $p_4$  (E2M1),  $p_6$  (E3M2), and  $p_8$  across Llama3.1-8B. We evaluate 32 samples selected from WikiText2 (Merity et al. 2016) and the Pile dataset (Gao et al. 2020), covering batch sizes of 8, 16, 32, and 64, and sequence lengths of 512, 1024, 2048, and 4096. For each sample,  $p_4$ ,  $p_6$ , and  $p_8$  are computed over all linear layers. The figure reports the mean values and min-max ranges of  $p_4$ ,  $p_6$ , and  $p_8$  across all samples.

linear layer in Llama3.1-8B. The results are shown in Figure 4. We summarize three key observations:

**Layer-wise Adaptivity:** The proportions vary dynamically across layers, reflecting the diverse input distributions in each activation. This demonstrates that the mixed-precision allocation is layer-specific rather than fixed globally.

**FP4 Dominance:** The proportion  $p_4$  consistently exceeds 50%, indicating that FP4 computations dominate the mixed-precision workflow. This dominance contributes significantly to the computational efficiency of the model.

**Cross-Dataset Stability:** The variations of  $p_4$ ,  $p_6$ , and  $p_8$  across different datasets and sampling strategies are minimal, suggesting that the mixed-precision assignment remains relatively stable.

**Q3: How is channel assignment determined?** Online evaluation of channel division using Equation (6) would introduce significant runtime overhead. Instead, leveraging the observed stability of  $p_4$ ,  $p_6$ , and  $p_8$ , we pre-determine channel indices for each partition offline using calibration data.

To prioritize higher precision for more critical channels, we sort the activation channels by their absolute mean values. Specifically, for an activation tensor  $\mathbf{X} \in \mathbb{R}^{L \times I}$ , the channel-wise absolute mean is computed as:

$$\mathbf{M} = \left( \frac{1}{L} \sum_{i=1}^L |X_{i1}|, \frac{1}{L} \sum_{i=1}^L |X_{i2}|, \dots, \frac{1}{L} \sum_{i=1}^L |X_{iI}| \right) \quad (7)$$

Since channels with larger average magnitudes typically incur higher quantization errors, MicroMix assigns precision levels according to the sorted values in  $\mathbf{M}$ : channels with smaller  $\mathbf{M}$  values are quantized to MXFP4, followed by MXFP6 and MXFP8 in ascending order of their  $\mathbf{M}$  values.

### 3.2 Kernel Design

Low-bit quantization offers significant performance improvements but presents considerable challenges in kernel design, especially for mixed-precision and fine-grained schemes like MicroMix. Recent advancements in GPU architectures, particularly the increased throughput of Tensor Cores for low-bit floating-point operations, combined with underlying support for block-scaled formats, have diminished the competitive advantage of traditional INT-type and

GEMM quantization kernels. This simultaneously creates new opportunities for low-bit floating-point quantization.

**Mixed-precision Quantization.** Driven by the goal of deep algorithm-hardware integration, we have designed a mixed-precision, block-scaling quantization kernel for MicroMix. Complementing this, we adopt MXFP-type GEMM kernels from CUTLASS, resulting in a kernel suite that delivers both excellent performance and high accuracy.

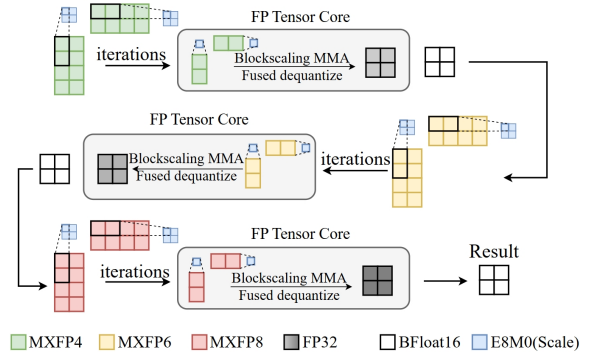


Figure 5: The fused GEMM kernel of MicroMix.

**Fine-grained Block-scaled Data Formats.** Quantization error is also influenced by the number of elements sharing a single scale factor. To fully harness the representational power of low-bit data types, fine-grained group quantization has become widely adopted and proven efficient in related works such as Atom and QuaRot. This used to be a tough trade-off between accuracy gains and dequantization overhead. However, the NVIDIA Blackwell architecture changes the game. Blackwell’s `tgen05.mma` instructions directly support new 4, 6, and 8-bit floating-point data types with integrated scale factors (known as MXFP formats), making block-scaled quantization a truly practical solution.

**GEMM Kernel.** As shown in Figure 5, the output matrix is divided into blocks within each GEMM kernel, with iterations for each block performed along the  $K$  dimension. After loading fragments of input matrices and their scale factors into Shared Memory or Tensor Memory, MMA instructions

fused with dequantization operations are continuously executed on Tensor Cores. These operations accumulate FP32 partial sums into the BFloat16 result matrix. The process is highly decoupled, as matrices of specific data types invoke their corresponding GEMM kernels. This design allows for easy adjustment of data type categories and their ratios.

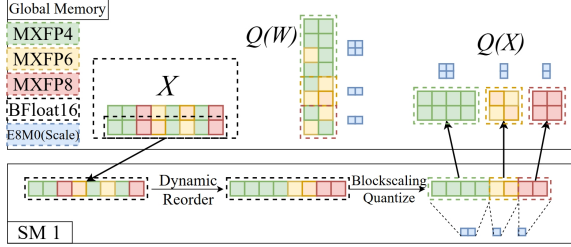


Figure 6: The fused reorder-and-quantize operation. The quantization of weights is one-time cost and could be performed offline.

**Quantization Kernel.** Mixed-precision quantization often faces irregular memory access, leading to significant performance degradation. To tackle this, MicroMix adopts a strategy similar to Atom and RPTQ (Yuan et al. 2023) by reordering channels to enable regular memory access. Our algorithm divides channels of activation into three distinct parts, to which we then apply block-wise scaling quantization in 32-element blocks. To ensure correct matrix multiplication, weights are correspondingly permuted to match the reordered activations before undergoing a similar three-part block-wise scaling quantization. Crucially, the reordering and quantization of activations must occur dynamically, while these processes for weights can be handled offline as a pre-processing step. To mitigate the overhead of dynamic reordering, we employ a kernel fusion technique (see Figure 6), which combines the quantization and reordering operations into a single kernel.

**Integration into Transformer Blocks.** The Transformer block is the basic unit of modern LLMs built on the Transformer architecture; for example, models like Llama and Qwen are constructed by stacking multiple Transformer blocks. In our approach, we replace all linear layers within the Transformer block with MicroMix kernels, as depicted in Figure 7. To boost efficiency, we perform a single reorder-and-quantize operation after LayerNorm. This is possible because the activation matrix processed by LayerNorm is shared across multiple subsequent linear layers. Additionally, we’ve integrated FlashInfer (Ye et al. 2024) to accelerate KV Cache operations and Attention calculations, further enhancing performance.

## 4 Experiments

### 4.1 Experimental Setup

**Quantization.** Following the Microscaling data format setup, MicroMix performs block-wise symmetric quantization with a block size of 32 for both weights and activations, using the E8M0 scaling format. The data formats are

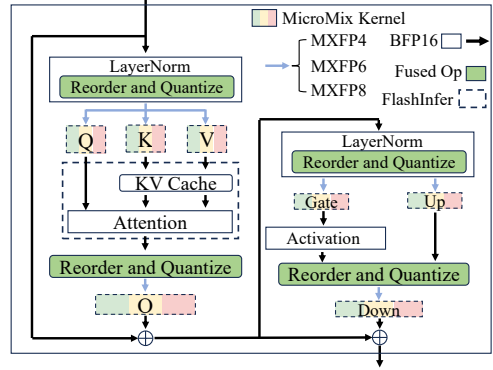


Figure 7: Precision mapping of MicroMix for a Transformer block in LLM.

MXFP8 (E4M3), MXFP6 (E3M2), MXFP4 (E2M1) respectively. To assign channels to three precision groups, we use 32 sequences of length 2048 from the WikiText2 dataset (Merity et al. 2016). A summary of the quantized model information is provided in Table 1.

Models	Avg. Bits	Memory	Time
Llama3.1-8B	5.51	5.09GB	179s
Qwen2.5-32B	5.22	24.54GB	406s
Qwen2.5-Coder-7B-Instruct	5.44	4.81GB	143s
Qwen2.5-Coder-14B-Instruct	5.54	9.10GB	260s
Qwen2.5-Coder-32B-Instruct	5.18	24.53GB	406s
Qwen2.5-Math-7B-Instruct	5.16	4.79GB	143s

Table 1: Average bit-width per element and memory consumption of quantized weights across all evaluated models. “Time” denotes the total offline time cost, including reordering and quantization of the original model.

**Baselines.** We compare MicroMix against three INT-based weight-activation quantization methods: Atom (Zhao et al. 2024), QUIK (Ashkboos et al. 2023), QuaRot (Ashkboos et al. 2024) and one MX quantization method: AMXFP4 (Lee et al. 2025). All baselines are reproduced on the Llama (Grattafiori et al. 2024) and Qwen (Qwen et al. 2025) models. Since INT-based methods’ kernels do not support progressive group quantization as used in Microscaling formats, we follow their original designs and implement them with standard INT group quantization of size 128 and FP16 scaling factors. AMXFP4 combines asymmetric per-block quantization of size 32 with MXFP4. More implementation details can be found in Appendix C.1.

**Benchmarks.** For zero-shot evaluation, we use ARC\_C (Clark et al. 2018), Lambada (Paperno et al. 2016), Winogrande (Sakaguchi et al. 2019), BoolQ (Clark et al. 2019), and PIQA (Lourie et al. 2021). For five-shot accuracy, we adopt MMLU (Hendrycks et al. 2021). WikiText2 (Merity et al. 2016) is used to evaluate perplexity (PPL). Additionally, we assess the Code and Math capabilities of the Qwen2.5 model series. Code benchmark is Human-Eval (Chen et al. 2021), while Math benchmarks cover GSM8K

Model	Method	0-shot						5-shot	WikiText2
		ARC.C	BoolQ	Lambada	PIQA	Winogrande	Avg.		
Llama3.1-8B	FP16	51.28	82.05	75.80	80.03	73.64	72.56	65.40	5.60
	QuaRot	46.42	76.24	68.48	77.91	<b>70.96</b>	68.00	55.23	6.98
	QUIK	44.62	77.09	73.28	77.09	69.19	68.05	56.65	7.29
	Atom	<b>50.17</b>	76.15	69.45	78.02	70.01	68.76	58.05	6.79
	AMXFP4	43.77	74.80	71.12	75.19	66.85	66.34	53.79	7.49
	MicroMix	49.74	<b>80.18</b>	<b>72.64</b>	<b>78.29</b>	70.80	<b>70.33</b>	<b>58.47</b>	<b>6.72</b>
Qwen2.5-32B	FP16	55.89	87.46	76.21	82.26	75.93	75.55	83.32	4.46
	QuaRot	53.08	84.77	74.89	80.96	73.14	73.36	79.39	5.86
	QUIK	52.90	85.87	74.21	80.36	71.82	73.03	78.89	5.92
	Atom	54.78	86.54	75.92	81.45	73.48	74.43	79.54	5.89
	AMXFP4	51.54	<b>87.09</b>	75.24	80.85	73.51	73.64	79.96	5.85
	MicroMix	<b>54.95</b>	85.60	<b>77.24</b>	<b>81.61</b>	<b>73.64</b>	<b>74.60</b>	<b>80.91</b>	<b>5.81</b>

Table 2: Zero-shot, few-shot accuracy ( $\uparrow$ ) and perplexity ( $\downarrow$ ) of Llama3.1-8B and Qwen2.5-32B, using lm-eval (Gao et al. 2024).

(Cobbe et al. 2021), MMLU-STEM (Hendrycks et al. 2021), CMATH (Wei et al. 2023) and CN Middle School 24.

## 4.2 Main Results

Table 2 reports the results on zero-shot and five-shot accuracy, as well as perplexity, for MicroMix and baseline methods. On zero-shot tasks, MicroMix retains over 95% of FP16 accuracy and achieves state-of-the-art results on Lambada, PIQA, and the average score across tasks. On MMLU (five-shot), MicroMix maintains over 90% of FP16 accuracy, and its perplexity degradation on WikiText2 remains within 20%.

**Code benchmark.** As shown in Figure 8, MicroMix achieves comparable or better accuracy than Atom on the 7B, 14B, and 32B models. Compared to FP16, the accuracy drop is kept within 3%, and MicroMix even outperforms FP16 on the 32B model.

**Math benchmarks.** Table 3 shows that MicroMix incurs less than a 2% accuracy drop compared to FP16, and surpasses FP8 on MMLU-STEM and CN Middle School 24.

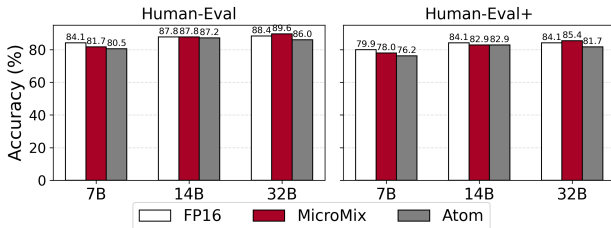


Figure 8: Accuracy ( $\uparrow$ ) of Qwen2.5-Coder-{7B, 14B, 32B}-Instruct on Code benchmark: Human-Eval.

## 4.3 Ablation Studies

In this section, we analyze the potential impact of different data formats and calibration datasets on MicroMix.

**MXFP6 and MXFP8 Variants.** We evaluate multiple variants of MXFP6 (E2M3 and E3M2) and MXFP8

Model	Method	EN		ZH	
		GSM8K	M.S	CMATH	CNMS
7B	FP16	95.8	77.8	91.5	72.3
	FP8	95.5	68.7	91.7	74.3
	MicroMix	94.5	77.1	90.8	75.2

Table 3: Accuracy ( $\uparrow$ ) of Qwen2.5-Math-7B-Instruct on English benchmarks: GSM8K, M.S (MMLU-STEM) and Chinese benchmarks: CMATH, CNMS (CN Middle School 24). FP8 is implemented by vLLM (Kwon et al. 2023).

(E5M2 and E4M3) on zero-shot accuracy and perplexity. As shown in Table 4, the combination of E4M3 (MXFP8) and E3M2 (MXFP6) achieves the best overall performance, with E5M2+E3M2 performing similarly. The results suggest that for high-precision formats like MXFP8, the specific exponent/mantissa configuration has limited impact. However, for lower-bit formats, the E3M2 configuration in MXFP6 improves accuracy by up to 5% compared to E2M3.

MXFP8	MXFP6	WG	Lambada	PIQA	Wiki
E5M2	E3M2	70.09	70.62	77.64	6.77
	E2M3	67.01	69.24	76.99	7.12
E4M3	E3M2	70.33	72.64	78.29	6.72
	E2M3	69.77	70.62	77.2	7.05

Table 4: Zero-shot accuracy ( $\uparrow$ ) on Winogrande (WG), Lambada, PIQA, and perplexity ( $\downarrow$ ) on Wiki (WikiText2), using different exponent and mantissa bits for MXFP6 and MXFP8 on Llama3.1-8B. MXFP4 is E2M1 consistently.

**Impact of Calibration Datasets.** MicroMix determines channel partitioning offline on a calibration dataset. To assess the robustness of this process, we test different calibration datasets, including the language datasets WikiText2 and Pile, and the code dataset Human-Eval. As shown in Table 5,

zero-shot and perplexity results remain stable across datasets with performance fluctuations within approximately 1%.

Calib Data	ARC.C	BoolQ	Lambada	PIQA	Wiki
WikiText2	56.66	83.00	74.17	80.63	5.8
Pile	55.89	83.58	74.48	80.20	5.91
Human-Eval	55.46	84.31	75.12	79.49	5.94

Table 5: Zero-shot accuracy ( $\uparrow$ ) on ARC.C, BoolQ, Lambada, PIQA, and perplexity ( $\downarrow$ ) on Wiki (WikiText2) of MicroMix on different datasets using Qwen2.5-14B.

**Time Breakdown by Component.** We measure the proportion of total runtime spent on each component, including the reorder-and-quantize operation, the FP4, FP6, and FP8 GEMM kernels, on an RTX 5090 GPU (see Table 7 in Appendix C.2 for details). Across input lengths ranging from 128 to 4096 tokens, the reorder-and-quantize step takes 7% to 17% of the total time, FP4 GEMM accounts for 20% to 31%, FP6 GEMM for 29% to 44%, and FP8 GEMM for 18% to 30%.

#### 4.4 Efficiency Evaluation

In this section, we evaluate the efficiency of MicroMix from two aspects: (1) The computing speed of a single kernel; (2) Prefill speed of the transformer block. (3) End-to-end throughput. The used framework of (2) and (3) is adapted from Huggingface (Wolf et al. 2020), with all linear layers replaced by MicroMix kernels. We select two Blackwell architecture GPUs: RTX 5070Ti laptop and RTX 5090 to test the applicability of MicroMix. Meanwhile, since MicroMix employs a non-fixed number of 4,6, and 8-bit channels, all experiments of kernels and transformer blocks have marked the min-max range and mean value curves. For comparison, we choose strong baselines from TensorRT-LLM, including TensorRT-FP8 (per-tensor), W4A16 (per-token), and FP16.

**Kernel Efficiency.** We test the computational latency of MicroMix kernel on different sequence lengths and hidden sizes. As shown in Figure 9, the speed of MicroMix kernel is consistently faster than TRT-FP8 on two GPUs of different settings. Compared with TRT-FP8, MicroMix achieved an acceleration of 8% to 46% on the 5070Ti laptop and 16% to 46% on the 5090.

**Transformer Block Efficiency.** As shown in Figure 10, we test three LLMs of sequence length 2048 and different batch sizes on 5090. Compared to TRT-FP8, results show that the average speed of the transformer block integrated with MicroMix kernel has increased by 6% to 15% for Llama3.1-8B, by 16% to 27% for Qwen2.5-14B, and by 21% to 29% for Qwen2.5-32B.

**End-to-end Throughput.** Figure 11 presents the end-to-end inference throughput and peak memory usage of Llama2-7B and Llama3.1-8B on 5090 with a batch size of 32 and sequence length of 2048. Compared to TensorRT-FP8, MicroMix improves inference throughput by 3.5% to 9.7% and reduces peak memory usage by 19.7% to 20.0%.

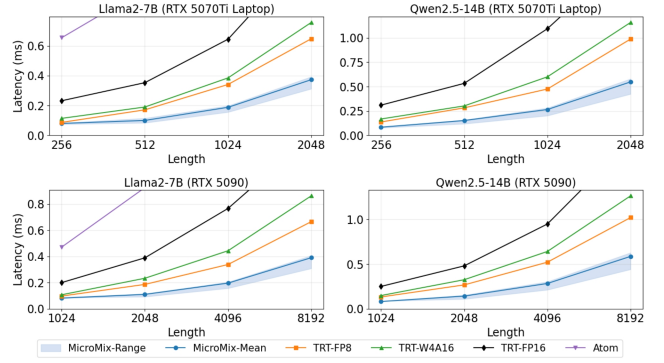


Figure 9: Computational latency of a single kernel. The input matrices have shapes of  $\text{Length} \times K$  and  $K \times N$ , where  $K = N = 4096$  for Llama2-7B and  $K = N = 5120$  for Qwen2.5-14B. Since MicroMix uses dynamic precision ratios, "MicroMix-Range" denotes the latency span from the fastest to the slowest time.

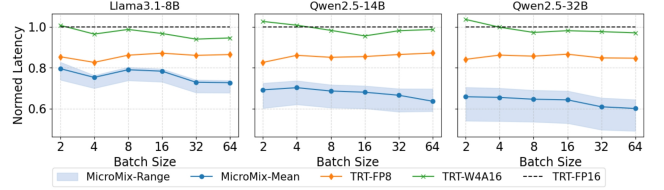


Figure 10: Different transformer blocks' normed speed of prefill length 2048 on RTX 5090. "Micromix-Range" shows the min to max normed speed range.

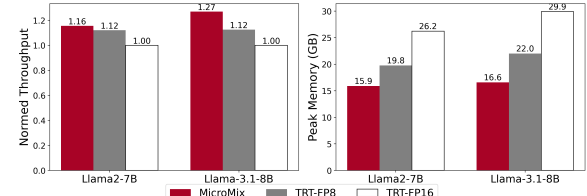


Figure 11: End-to-end comparison between MicroMix and TensorRT-LLM baselines. Left: Normed Throughput. Right: Peak Memory.

## 5 Related Works

**Mixed-precision quantization** retains outliers in higher bit-widths while quantizing the remaining elements to lower bit-widths (Dettmers et al. 2022; Saxena et al. 2025; Ashkboos et al. 2023; Hooper et al. 2025). The central challenge is designing efficient fused GEMM kernel. Atom (Zhao et al. 2024) achieves state-of-the-art performance by preserving 128 outlier channels in INT8 and quantizing the rest to INT4. Although Atom demonstrated a  $7.73 \times$  speedup over FP16 on the RTX 4090, its current kernel is limited to Llama2-7B and can only handle up to 128 high-precision channels. Unlike previous approaches that use a fixed number of high-precision channels for all linear layers, our method enables flexible, fine-grained mixed-precision

configurations, and is specifically designed to leverage the advantages of Microscaling data formats.

**Applications of Microscaling data formats.** Recent works (Darvish Rouhani et al. 2023b; Sharify et al. 2024a,b) begin to study the applications of MX in both training and inference. AMXFP4 (Lee et al. 2025) handles outliers and asymmetries in activation by introducing asymmetric shared scales. Furthermore, Chen et al. (2025) significantly improved the FP4 training accuracy of Vision Transformers by identifying and solving the weight oscillation problem in forward propagation. MicroScopiQ (Akshat Ramachandran 2025) optimizes the quantization by combining pruning with outlier-aware miniaturization. Although these works have made significant progress in the inference and training of low-width MX formats, there is still a lack of systematic work on using microscaling data formats for general mixed-precision quantization.

## 6 Conclusion

In this paper, we present MicroMix, a co-designed mixed-precision quantization algorithm and kernel that supports MXFP4, MXFP6, and MXFP8 formats. Our algorithm introduces the quantization threshold to identify elements that incur excessive quantization error at the target bit width. We also propose an offline calibration strategy to determine the optimal channel assignments for each precision level on calibration dataset. To enable efficient inference, we design a matrix multiplication kernel that integrates three GEMM precisions and a fused reorder-and-quantize operation. MicroMix achieves significant speedups over TensorRT baselines on both edge (RTX 5070Ti laptop) and server-level (RTX 5090) GPUs across various configurations.

## References

Akshat Ramachandran, T. K., Souvik Kundu. 2025. MicroScopiQ: Accelerating Foundational Models through Outlier-Aware Microscaling Quantization. *arXiv:2411.05282*.

Ashkboos, S.; Markov, I.; Frantar, E.; Zhong, T.; Wang, X.; Ren, J.; Hoefler, T.; and Alistarh, D. 2023. QUIK: Towards End-to-end 4-Bit Inference on Generative Large Language Models. *arXiv preprint arXiv:2310.09259*.

Ashkboos, S.; Mohtashami, A.; Croci, M. L.; Li, B.; Cameron, P.; Jaggi, M.; Alistarh, D.; Hoefler, T.; and Hensman, J. 2024. QuaRot: Outlier-Free 4-Bit Inference in Rotated LLMs. In *The Thirty-eighth Annual Conference on Neural Information Processing Systems*, 33: 1877–1901.

Brown, T. B.; Mann, B.; Ryder, N.; Subbiah, M.; Kaplan, J. D.; Dhariwal, P.; Neelakantan, A.; Shyam, P.; Sastry, G.; Askell, A.; et al. 2020. Language Models are Few-Shot Learners. *Advances in Neural Information Processing Systems*, 33: 1877–1901.

Chen, M.; Tworek, J.; Jun, H.; Yuan, Q.; de Oliveira Pinto, H. P.; Kaplan, J.; Edwards, H.; Burda, Y.; Joseph, N.; Brockman, G.; Ray, A.; Puri, R.; Krueger, G.; Petrov, M.; Khlaaf, H.; Sastry, G.; Mishkin, P.; Chan, B.; Gray, S.; Ryder, N.; Pavlov, M.; Power, A.; Kaiser, L.; Bavarian, M.; Winter, C.; Tillet, P.; Such, F. P.; Cummings, D.; Plappert, M.; Chantzis, F.; Barnes, E.; Herbert-Voss, A.; Guss, W. H.; Nichol, A.; Paino, A.; Tezak, N.; Tang, J.; Babuschkin, I.; Balaji, S.; Jain, S.; Saunders, W.; Hesse, C.; Carr, A. N.; Leike, J.; Achiam, J.; Misra, V.; Morikawa, E.; Radford, A.; Knight, M.; Brundage, M.; Murati, M.; Mayer, K.; Welinder, P.; McGrew, B.; Amodei, D.; McCandlish, S.; Sutskever, I.; and Zaremba, W. 2021. Evaluating Large Language Models Trained on Code.

Chen, Y.; Xi, H.; Zhu, J.; and Chen, J. 2025. Oscillation-Reduced MXFP4 Training for Vision Transformers. *arXiv:2502.20853*.

Clark, C.; Lee, K.; Chang, M.-W.; Kwiatkowski, T.; Collins, M.; and Toutanova, K. 2019. BERT: Pre-training of Deep Bidirectional Transformers for Language Understanding. *arXiv preprint arXiv:1810.04805*.

Clark, P.; Cowhey, I.; Etzioni, O.; Khot, T.; Sabharwal, A.; Schoenick, C.; and Tafjord, O. 2018. Think you have Solved Question Answering? Try ARC, the AI2 Reasoning Challenge. *arXiv:1803.05457v1*.

Cobbe, K.; Kosaraju, V.; Bavarian, M.; Chen, M.; Jun, H.; Kaiser, L.; Plappert, M.; Tworek, J.; Hilton, J.; Nakano, R.; Hesse, C.; and Schulman, J. 2021. Training Verifiers to Solve Math Word Problems. *arXiv preprint arXiv:2110.14168*.

Darvish Rouhani, B.; Garegrat, N.; Savell, T.; More, A.; Han, K.-N.; Zhao, M.; Ritchie and Hall; Klar, J.; Chung, E.; Yu, Y.; Schulte, M.; Wittig, R.; Bratt, I.; Stephens, N.; Milanovic, J.; Brothers, J.; Dubey, P.; Cornea, M.; Heinecke, A.; Rodriguez, A.; Langhammer, M.; Deng, S.; Naumov, M.; Micikevicius, P.; Siu, M.; and Verrilli, C. 2023a. OCP Microscaling (MX) Specification. *Open Compute Project*.

Darvish Rouhani, B.; Zhao, R.; More, A.; Hall, M.; Khodamoradi, A.; Deng, S.; Choudhary, D.; Cornea, M.; Dellinger, E.; Denolf, K.; Dusan, S.; Elango, V.; Golub, M.; Heinecke, A.; James-Roxby, P.; Jani, D.; Kolhe, G.; Langhammer, M.; Li, A.; Melnick, L.; Mesmakhosroshahi, M.; Rodriguez, A.; Schulte, M.; Shafipour, R.; Shao, L.; Siu, M.; Dubey, P.; Micikevicius, P.; Naumov, M.; Verrilli, C.; Wittig, R.; Burger, D.; and Chung, E. 2023b. Microscaling Data Formats for Deep Learning. *arXiv:2310.10537*.

Dettmers, T.; Lewis, M.; Belkada, Y.; and Zettlemoyer, L. 2022. LLM.int8(): 8-bit Matrix Multiplication for Transformers at Scale. *arXiv:2208.07339*.

Frantar, E.; Ashkboos, S.; Hoefler, T.; and Alistarh, D. 2023. GPTQ: Accurate Post-Training Quantization for Generative Pre-trained Transformers. *arXiv:2210.17323*.

Gao, L.; Biderman, S.; Black, S.; Golding, L.; Hoppe, T.; Foster, C.; Phang, J.; He, H.; Thite, A.; Nabeshima, N.; Presser, S.; and Leahy, C. 2020. The Pile: An 800GB Dataset of Diverse Text for Language Modeling. *arXiv:2101.00027*.

Gao, L.; Tow, J.; Abbasi, B.; Biderman, S.; Black, S.; DiPofi, A.; Foster, C.; Golding, L.; Hsu, J.; Le Noac'h, A.; Li, H.; McDonell, K.; Muennighoff, N.; Ociepa, C.; Phang, J.; Reynolds, L.; Schoelkopf, H.; Skowron, A.; Sutawika, L.; Tang, E.; Thite, A.; Wang, B.; Wang, K.; and Zou, A. 2024. The Language Model Evaluation Harness.

Grattafiori, A.; Dubey, A.; Jauhri, A.; Pandey, A.; Kadian, A.; Al-Dahle, A.; Letman, A.; and Akhil Mathur, e. a. 2024. The Llama 3 Herd of Models. *arXiv:2407.21783*.

Hendrycks, D.; Burns, C.; Basart, S.; Zou, A.; Mazeika, M.; Song, D.; and Steinhardt, J. 2021. Measuring Massive Multitask Language Understanding. *Proceedings of the International Conference on Learning Representations (ICLR)*.

Hooper, C.; Sakr, C.; Keller, B.; Venkatesan, R.; Keutzer, K.; Shao, S.; and Khailany, B. 2025. FGMP: Fine-Grained Mixed-Precision Weight and Activation Quantization for Hardware-Accelerated LLM Inference. *arXiv:2504.14152*.

Kwon, W.; Li, Z.; Zhuang, S.; Sheng, Y.; Zheng, L.; Yu, C. H.; Gonzalez, J. E.; Zhang, H.; and Stoica, I. 2023. Efficient Memory Management for Large Language Model Serving with PagedAttention. In *Proceedings of the ACM SIGOPS 29th Symposium on Operating Systems Principles*.

Lee, J.; Park, J.; Kim, J.; Kim, Y.; Oh, J.; Oh, J.; and Choi, J. 2025. AMXFP4: Taming Activation Outliers with Asymmetric Microscaling Floating-Point for 4-bit LLM Inference. *arXiv:2411.09909*.

Lin, J.; Tang, J.; Tang, H.; Yang, S.; Chen, W.-M.; Wang, W.-C.; Xiao, G.; Dang, X.; Gan, C.; and Han, S. 2024. AWQ: Activation-aware Weight Quantization for LLM Compression and Acceleration. In *MLSys*.

Lourie, N.; Bras, R. L.; Bhagavatula, C.; and Choi, Y. 2021. UNICORN on RAINBOW: A Universal Commonsense Reasoning Model on a New Multitask Benchmark. *arXiv:2103.13009*.

Merity, S.; Xiong, C.; Bradbury, J.; and Socher, R. 2016. Pointer Sentinel Mixture Models. *CoRR*, abs/1609.07843.

Paperno, D.; Kruszewski, G.; Lazaridou, A.; Pham, N. Q.; Bernardi, R.; Pezzelle, S.; Baroni, M.; Boleda, G.; and Fernandez, R. 2016. The LAMBADA dataset: Word prediction requiring a broad discourse context. In *Proceedings of the 54th Annual Meeting of the Association for Computational Linguistics (Volume 1: Long Papers)*, 1525–1534. Berlin, Germany: Association for Computational Linguistics.

Qwen; ; Yang, A.; Yang, B.; Zhang, B.; Hui, B.; Zheng, B.; Yu, B.; Li, C.; Liu, D.; Huang, F.; Wei, H.; Lin, H.; Yang, J.; Tu, J.; Zhang, J.; Yang, J.; Yang, J.; Zhou, J.; Lin, J.; Dang, K.; Lu, K.; Bao, K.; Yang, K.; Yu, L.; Li, M.; Xue, M.; Zhang, P.; Zhu, Q.; Men, R.; Lin, R.; Li, T.; Tang, T.; Xia, T.; Ren, X.; Ren, X.; Fan, Y.; Su, Y.; Zhang, Y.; Wan, Y.; Liu, Y.; Cui, Z.; Zhang, Z.; and Qiu, Z. 2025. Qwen2.5 Technical Report. *arXiv:2412.15115*.

Sakaguchi, K.; Bras, R. L.; Bhagavatula, C.; and Choi, Y. 2019. WinoGrande: An Adversarial Winograd Schema Challenge at Scale. *arXiv:1907.10641*.

Saxena, U.; Sharify, S.; Roy, K.; and Wang, X. 2025. ResQ: Mixed-Precision Quantization of Large Language Models with Low-Rank Residuals. *arXiv:2412.14363*.

Sharify, S.; Saxena, U.; Xu, Z.; Yazar, W.; Soloveychik, I.; and Wang, X. 2024a. Post Training Quantization of Large Language Models with Microscaling Formats. *arXiv:2405.07135*.

Sharify, S.; Saxena, U.; Xu, Z.; Yazar, W.; Soloveychik, I.; and Wang, X. 2024b. Post Training Quantization of Large Language Models with Microscaling Formats. *arXiv:2405.07135*.

Shen, X.; Dong, P.; Lu, L.; Kong, Z.; Li, Z.; Lin, M.; Wu, C.; and Wang, Y. 2023. Agile-Quant: Activation-Guided Quantization for Faster Inference of LLMs on the Edge. *arXiv:2312.05693*.

Vaswani, A.; Shazeer, N.; Parmar, N.; Uszkoreit, J.; Jones, L.; Gomez, A. N.; Kaiser, L.; and Polosukhin, I. 2023. Attention Is All You Need. *arXiv:1706.03762*.

Wei, T.; Luan, J.; Liu, W.; Dong, S.; and Wang, B. 2023. CMATH: Can Your Language Model Pass Chinese Elementary School Math Test? *arXiv:2306.16636*.

Wolf, T.; Debut, L.; Sanh, V.; Chaumond, J.; Delangue, C.; Moi, A.; Cistac, P.; Rault, T.; Louf, R.; Funtowicz, M.; Davison, J.; Shleifer, S.; von Platen, P.; Ma, C.; Jernite, Y.; Plu, J.; Xu, C.; Scao, T. L.; Gugger, S.; Drame, M.; Lhoest, Q.; and Rush, A. M. 2020. Transformers: State-of-the-Art Natural Language Processing. In *Proceedings of the 2020 Conference on Empirical Methods in Natural Language Processing: System Demonstrations*, 38–45. Online: Association for Computational Linguistics.

Xiao, G.; Lin, J.; Seznec, M.; Wu, H.; Demouth, J.; and Han, S. 2024. SmoothQuant: Accurate and Efficient Post-Training Quantization for Large Language Models. *arXiv:2211.10438*.

Yao, Z.; Aminabadi, R. Y.; Zhang, M.; Wu, X.; Li, C.; and He, Y. 2022. ZeroQuant: Efficient and Affordable Post-Training Quantization for Large-Scale Transformers. *arXiv:2206.01861*.

Ye, Z.; Chen, L.; Lai, R.; Zhao, Y.; Zheng, S.; Shao, J.; Hou, B.; Jin, H.; Zuo, Y.; Yin, L.; Chen, T.; and Ceze, L. 2024. Accelerating Self-Attentions for LLM Serving with FlashInfer.

Yuan, Z.; Niu, L.; Liu, J.; Liu, W.; Wang, X.; Shang, Y.; Sun, G.; Wu, Q.; Wu, J.; and Wu, B. 2023. RPTQ: Reorder-based Post-training Quantization for Large Language Models. *arXiv:2304.01089*.

Zhao, Y.; Lin, C.-Y.; Zhu, K.; Ye, Z.; Chen, L.; Zheng, S.; Ceze, L.; Krishnamurthy, A.; Chen, T.; and Kasikci, B. 2024. Atom: Low-Bit Quantization for Efficient and Accurate LLM Serving. In Gibbons, P.; Pekhimenko, G.; and Sa, C. D., eds., *Proceedings of Machine Learning and Systems*, volume 6, 196–209.

## A Microscaling (MX)

According to Darvish Rouhani et al. (2023a), we give some supplementary information of MX in this section. An MX-compliant format is consisted of three components: scaling block size  $k$ ,  $k$  scalar elements  $\{x_i\}_{i=1}^k$  and a shared scale  $s$  in E8M0 format (see Figure 12). Here,  $\{x_i\}_{i=1}^k$  is already quantized, so the original value is  $\{sx_i\}_{i=1}^k$ . The specific parameters of MX data formats are shown in Table 6. More details on MX please refer to OCP Microscaling Specification (Darvish Rouhani et al. 2023a).

Format Name	Element Bits ( $d$ )	Element Data Type	Exponent Bias ( $b$ )	Max Normal	Scaling Block Size ( $k$ )	Scale Data Type	Scale Bits ( $w$ )
MXFP8	8	FP8 (E5M2)	15	$\pm 57344$	32	E8M0	8
		FP8 (E4M3)	7	$\pm 448$			
MXFP6	6	FP6 (E3M2)	3	$\pm 28$	32	E8M0	8
		FP6 (E2M3)	1	$\pm 7.5$			
MXFP4	8	FP4 (E2M1)	1	$\pm 6$	32	E8M0	8
MXINT8	8	INT8	N/A	$\pm 163/64$	32	E8M0	8

Table 6: Format names and parameters of concrete MX-compliant formats (Darvish Rouhani et al. 2023a).

Length	Reorder-and-quantize	FP4 GEMM	FP6 GEMM	FP8 GEMM
128	7.9%	31.5%	29.9%	30.7%
256	9.7%	30.6%	29.8%	29.8%
512	11.8%	29.9%	29.1%	29.1%
1024	14.3%	27.1%	30.7%	27.9%
2048	17.0%	21.6%	40.7%	20.6%
4096	16.9%	20.9%	44.0%	18.2%

Table 7: The proportion of runtime for each part on RTX 5090.

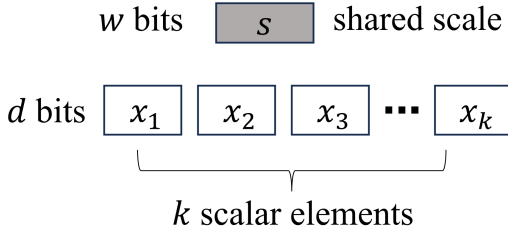


Figure 12: A schematic diagram of the basic unit of Microscaling block. The block encodes the original  $k$  values  $s x_i$  into  $k$  elements in MX and a shared scale  $s$ .

## B Quantization Error Analysis

### B.1 Observations

In this section, we discuss the quantization error in detail. We observe the variation relationship between the accuracy of the quantization model and the quantization error, which supplements the deficiency in the description of the continuity relationship between accuracy and error in previous works.

Given a FP16 tensor  $\mathbf{X} \in \mathbb{R}^{1 \times I}$ ,  $\forall X_i \in \mathbf{X}$ , the quantization error  $E(X_i)$  between  $Q(X_i)$  and  $X_i$  is:

$$E(X_i) = |X_i - Q(X_i)| = |X_i - \text{round}(\frac{X_i}{s})s| = \gamma \cdot s \quad (8)$$

where  $\gamma = |\text{round}(X_i/s) - X_i/s|$  is the rounding error. INT quantization is similar to FP quantization:

$$Q(X_i) = \text{round}(\frac{X_i}{s}), s = \frac{\max(|\mathbf{X}|)}{q_{max}} \quad (9)$$

where  $\text{round}(\cdot)$  is rounding to the nearest INT value and  $q_{max} = 2^{n-1} - 1$  is the maximum value of INT range. For INT format, there is  $\gamma \in [0, 0.5]$ , so we can get the quantization error upper bound  $\bar{E}(X_i)$  of INT format:

$$\begin{aligned} E(X_i) &= \gamma \cdot s \leq 0.5 \cdot s \\ &= 0.5 \cdot \frac{\max(|\mathbf{X}|)}{2^{n-1} - 1} = \frac{\max(|\mathbf{X}|)}{2^n - 2} = \bar{E}(X_i) \end{aligned} \quad (10)$$

in particular, for INT8:

$$\bar{E}(X_i)_{INT8} = \frac{\max(|\mathbf{X}|)}{254} \quad (11)$$

We reformulate Equation (11) as following:

$$\bar{E}(X_i) = \frac{\max(|\mathbf{X}|)}{2 \cdot q_{max}} \quad (12)$$

Then we control  $q_{max}$  to observe the relationship between the quantized model accuracy and the quantization error upper bound, as shown in Figure 13. We have three observations:

(1) The curve in Figure 13. clearly illustrates how model accuracy varies with quantization error. In general, the accuracy of the model decreases with the increase of the upper bound of the quantization error.

(2) There is a “Stable Stage” for each model maintaining high accuracy of variation  $q_{max}$ , INT8 ( $q_{max}=127$ ) is located in this stage. For all four models, INT8 is a high-precision format.

(3) When  $q_{max}$  is below a threshold, the accuracy of quantized model degrades significantly, which we name as “Decline Stage”, and INT4 ( $q_{max}=7$ ) is located at the end of this stage.

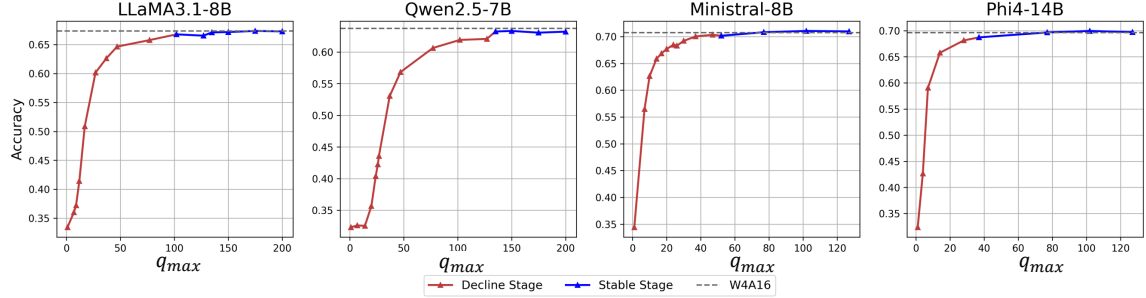


Figure 13: After quantizing weights to INT4 using per-channel symmetric quantization, the zero-shot average accuracy of the models on Winograde, PIQA, BoolQ, ARC\_C, and Lambda changes with  $q_{max}$ . The quantization process of activations corresponding to different  $q_{max}$  is implemented through fake-quant simulation. A lower value of  $q_{max}$  corresponds to a higher upper bound on the quantization error.

In conclusion, enhancing the accuracy of a quantized model requires reducing its quantization error to bring it within the stable stage. The relationship between the quantization error upper bound and the model accuracy inspires us to divide values into three parts from the view of quantization error upper bound.

## B.2 Derivations

In this section, we show the detailed derivation processes of quantization threshold, which is based on the motivation of controlling the quantization error of MXFP4/MXFP6 below  $\bar{E}(X_i)_{INT8}$ .

The quantization error of MXFP4/MXFP6 is:

$$E(X_i)_{\{MXFP4, MXFP6\}} = \gamma \cdot 2^{\lfloor \log_2(\max(|\mathbf{X}|)) \rfloor - b} \quad (13)$$

Since the gap between adjacent FP values is not a constant, we use

$$\gamma = \frac{q_{max}}{2^{n-1}} \quad (14)$$

to approximately express the rounding error in Equation (13), where  $q_{max}$  is the maximum value of MXFP4/MXFP6. Substituting Equation (14) into Equation (13) gives:

$$\begin{aligned} E(X_i) &= \frac{q_{max}}{2^{n-1}} \cdot 2^{\lfloor \log_2(\max(|\mathbf{X}|)) \rfloor - b} \\ &\leq \frac{q_{max}}{2^{n-1}} \cdot 2^{\log_2(\max(|\mathbf{X}|)) - b} \\ &= \frac{q_{max}}{2^{n-1}} \cdot \frac{\max(|\mathbf{X}|)}{2^b} \end{aligned} \quad (15)$$

Let  $E(P_i)_{\{MXFP4, MXFP6\}} \leq \bar{E}(X_i)_{INT8}$ , we have:

$$\begin{aligned} E(P_i) &\leq \frac{q_{max}}{2^{n-1}} \cdot \frac{\max(|\mathbf{P}|)}{2^b} \leq \frac{\max(|\mathbf{X}|)}{254} \\ \max(|\mathbf{P}|) &\leq 2^b \cdot \frac{2^{n-1}}{q_{max}} \cdot \frac{\max(|\mathbf{X}|)}{254} \end{aligned} \quad (16)$$

From Equation (16), we have  $\mathbf{P}_4 \subset \mathbf{P}_6$ , then we remove the values of  $\mathbf{P}_4$  in  $\mathbf{P}_6$  to obtain the new  $\mathbf{P}_6$  satisfying:

$$T(4) = 2^1 \cdot \frac{2^{4-1}}{6} \cdot \frac{\max(|\mathbf{X}|)}{254} < \min(|\mathbf{P}_6|) \quad (17)$$

$$\max(|\mathbf{P}_6|) \leq 2^b \cdot \frac{2^{n-1}}{q_{max}} \cdot \frac{\max(|\mathbf{X}|)}{254} = T(6)$$

and  $\mathbf{P}_4$  satisfies  $\max(|\mathbf{P}_4|) \leq T(4)$ .

## C Supplementary Materials of Experiments

### C.1 Experimental Settings

In this section, we demonstrate some reproduction details. All INT baselines use symmetric quantization for both weights and activations.

**Quarot**<sup>1</sup>. The intermediate sizes of Qwen series models are not supported when obtaining the Hadamard matrix (18944 for 7B, 13824 for 14B, 27648 for 32B). Our solution is to remove the Hadamard transformation before Down-proj, and keep Down-proj in W8A8 as compensation. *a\_clip\_ratio* is 0.9, and *w\_clip* is used.

**Atom**<sup>2</sup>. The activation-sort metric is chosen as “hessian” according to Atom’s default settings. *a\_clip\_ratio* is 0.9, *w\_clip\_ratio* is 0.85 and *keeper\_size* is 128.

**QUIK**<sup>3</sup>. The value of *fp\_features\_num* is set to 128, following the settings used in QUIK. *w\_clip* is used and *int8\_down\_proj* is used.

**AMXFP4**<sup>4</sup>. We use the *fp4\_e2m1\_asym* element format as specified in AMXFP4. *scale\_bits* is 8 and *block\_size* is 32.

### C.2 Supplementary Results

Table 8 shows the results of Atom and QUIK directly applied to MXFP4 and MXFP8, with a significant performance drop compared to MicroMix. Since the kernels of Atom and QUIK do not support the MXFP format, we use the MicroMix kernel to keep the number of MXFP8 channels at 128 and 256 respectively.

We use the average values of  $p_4$ ,  $p_6$ , and  $p_8$  from Llama3.1-8B to compute the runtime breakdown of reorder-and-quantize, FP4 GEMM, FP6 GEMM, and FP8 GEMM relative to the total kernel time, as shown in Table 7. As the sentence length increases ( $> 1024$ ), although the proportion of  $p_6$  remains relatively small, the runtime share of FP6 GEMM steadily increases. This indicates that FP6 GEMM is comparatively slower than FP4 and FP8.

<sup>1</sup><https://github.com/spcl/QuaRot/tree/main>

<sup>2</sup><https://github.com/efeslab/Atom>

<sup>3</sup><https://github.com/IST-DASLab/QUIK>

<sup>4</sup><https://github.com/aiha-lab/MX-QLLM>

Methods	ARC_C	BoolQ	Lambada	PIQA	Wiki
FP16	51.28	82.05	75.80	80.03	5.60
Atom	43.60	76.36	66.52	75.57	8.02
QUIK	47.27	76.15	68.52	767.22	7.86
MicroMix	<b>49.74</b>	<b>80.18</b>	<b>72.64</b>	<b>78.29</b>	<b>6.72</b>

Table 8: Zero-shot accuracy ( $\uparrow$ ) and WikiText2 perplexity ( $\downarrow$ ) results of mixed-precision methods on MXFP formats using Llama3.1-8B.